Noise Behavior and Implementation of Interferometer-Based Broadband VNA

Mubarak, Faisal Ali; Romano, Rafaelle; Galatro, Luca; Mascolo, Vincenzo; Rietveld, Gert; Spirito, Marco

DOI
10.1109/TMTT.2018.2874667

Publication date
2019

Document Version
Final published version

Published in
IEEE Transactions on Microwave Theory and Techniques

Noise Behavior and Implementation of Interferometer-Based Broadband VNA

Faisal Ali Mubarak, *Member, IEEE*, Rafaelle Romano, Luca Galatro, *Student Member, IEEE*, Vincenzo Mascolo, Gert Rietveld, *Senior Member, IEEE*, and Marco Spirito, *Member, IEEE*

***Abstract*— This paper analyzes and accurately models the complex noise behavior of vector network analyzers (VNAs) when measuring large-mismatch devices and subsequently shows how the VNA measurement noise performance is enhanced through implementation of a high-speed, broadband, active RF interferometer module. The presented VNA noise model provides a solid framework, benchmarked by measurement data, to analyze existing RF interferometer approaches. The performance improvement of the proposed interferometer implementation is then benchmarked in terms of magnitude and phase stability of the renormalized impedance level. A test bench employing the novel add-on RF interferometer module is presented and demonstrated to achieve high-speed cancellation of the scattered wave over a broad frequency band. The first experiment shows ultralow noise in a 1–18 GHz broadband measurement of co-planar waveguide 0.5-Ω and 5-kΩ impedance standards. Employing the proposed hardware setup improves the noise uncertainty for the 5-kΩ impedance standard by a factor of 8 and 20 at 1 and 18 GHz, respectively. In the second experiment, a factor of 2 height-resolution enhancement is achieved in a scanning microwave microscope when the RF interferometer module is added to the instrument.**

***Index Terms*— Extreme impedance measurement, impedance mismatch, microwave interferometry, nanoelectronics, nanostructures, noise, vector network analyzer (VNA).**

I. Introduction

VECTOR network analyzers (VNAs) are the fundamental instruments used to characterize high-frequency (HF) devices, operating over a broad frequency range (currently up to 1.1 THz). The VNAs achieve an extremely low measurement noise by employing narrowband filtering on the down-converted signals and achieve a high-absolute measurement accuracy using vector correction [1], [2]. However, this low measurement noise and high accuracy is only achieved when measuring devices under test (DUTs) with impedance levels close to the VNA instrument impedance ($\mathbf{Z}_0$), commonly designed to be 50 Ω. When the DUT impedance deviates from $\mathbf{Z}_0$, the VNA measurement sensitivity degrades progressively [3]–[5] presenting up to two orders of magnitude lower resolution in highly mismatched conditions, shown in Fig. 1. This provides a considerable hinder in the characterization and modeling of upcoming nanotechnologies [6], [7], the next generations of absorbing materials [8] and transistors [9], [10], and the continuous downscaling of CMOS technologies to smaller structures, presenting extremely low parasitic components. In all these cases, the limited RF characterization capabilities of present state VNAs are regarded as one of the bottlenecks in the further development of these devices. A second example is the scanning microwave microscope (SMM) for accurate characterization of localized material properties. This highly promising RF-metrology technology shows a very significant degradation in sensitivity due to the highly mismatched measurement conditions [11], [12], which is overcome today by static resonant structure, thus limiting the frequency band operation of the SMM.

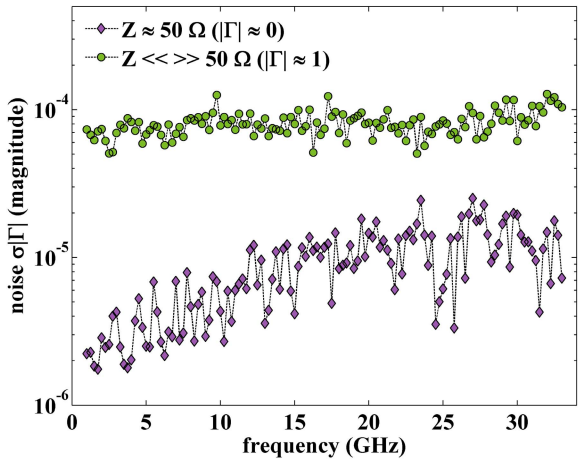

Fig. 1. VNA input reflection coefficient ($\mathbf{\Gamma}$) noise as a function of frequency for a high-reflection ($\mathbf{\Gamma} \approx 1$) and low-reflection ($\mathbf{\Gamma} \approx 0$) coefficient device.

The sensitivity degradation and larger trace noise in VNA measurements of non-50-Ω devices can be attributed, in a first approximation, to the presence of a scattered wave (i.e., **b**-wave) generated by the highly mismatched device.

Various techniques have been presented in the literature [13]–[16] to cancel the device generated **b**-wave by

Manuscript received April 13, 2018; revised August 12, 2018; accepted September 12, 2018. Date of publication December 7, 2018; date of current version January 4, 2019. This work was supported in part by the European Metrology Program for Innovation and Research (EMPIR) through the Microwave Measurement for Planar Circuits and Components Project under Grant 14IND02, in part by the Dutch Ministry of Economic Affairs, and in part by the EMPIR participating countries within the European Association of National Metrology Institutes and the European Union. *(Corresponding author: Faisal Ali Mubarak.)*

F. A. Mubarak, V. Mascolo, and G. Rietveld are with the Department of Research and Development, VSL-Dutch Metrology Institute, 2629 Delft, The Netherlands (e-mail: fmubarak@vsl.nl).

R. Romano and L. Galatro are with Vertigo Technologies B.V., 2629 Delft, The Netherlands.

M. Spirito is with the Electronics Research Department, Delft University of Technology, 2629 Delft, The Netherlands.

Color versions of one or more of the figures in this paper are available online at http://ieeexplore.ieee.org.

Digital Object Identifier 10.1109/TMTT.2018.2874667

superimposing a second wave ($\mathbf{b}_{\text{int}}$-wave), with opposite phase, effectively realizing an electrical high-frequency interferometer. In [13], the cancellation of the **b**-wave is achieved by employing 90° 3-dB couplers in combination with a high-reflection coefficient termination, comparable with the one of the DUT. The phase shift imbalance between the two couplers and their limited bandwidth bounds both the cancellation level that can be achieved as well as the frequency bandwidth of the method. In [14], the $\mathbf{b}_{\text{int}}$-wave was generated employing a power divider, a phase shifter, and an attenuator. Here, the moderate directivity of the power divider and the requirement to use a symmetric high-gamma device limits the stability of the cancellation wave, thus causing the $\mathbf{b}_{\text{int}}$-wave to vary with the DUT. Furthermore, [13] and [14] rely on passive components to achieve signal cancellation, thus limiting the maximum reflection $|\boldsymbol{\Gamma}|$ that could be optimized. A final disadvantage is that both the methods present a single-frequency cancellation approach as (slow) mechanical adjustments are required to the frequency shift cancellation condition.

In [15] and [16], the $\mathbf{b}_{\text{int}}$-wave is generated using active circuitry, either via a single-source technique with IQ-mixer steering configuration [15] or with phase-controllable dual synthesizers [16]. Both approaches allow to achieve high sensitivity over a broadband frequency range. However, in both implementations the $\mathbf{b}_{\text{int}}$-wave and the incident **a**-wave signals propagate, for a considerable length, over independent transmission lines, making the cancellation condition extremely sensitive to the relative phase fluctuations between the different propagation paths.

In this paper, we first present a detailed noise behavioral analysis for VNAs, providing insight into the sources of measurement noise and their interdependence under mismatched DUT conditions. Using the findings from noise behavioral analysis, the different passive and active interferometer techniques for VNAs, presented in literature are benchmarked for their achievable sensitivity and cancellation condition stability. The core part of this paper is the description of a novel implementation [17] of an active interferometer-based VNA with unprecedented noise and measurement speed, together with two experiments to validate and quantify the performance improvement of the new approach.

II. Noise in S-Parameter Measurements

The typical narrowband heterodyne architecture of VNAs allows to treat the random noise contribution as narrowband white noise. In [18]–[20] a black-box approach for VNA noise analysis is explored, from an operational perspective. In [19], the approach is limited to the noise assessment in matched conditions (i.e., $\boldsymbol{\Gamma} \approx 0$) and no solution is offered for highly mismatched cases (i.e., $\boldsymbol{\Gamma} > 0.9$). In [3] and [20] improved noise partitioning methods are proposed, giving a frequency-dependent noise evaluation over the entire $\boldsymbol{\Gamma}$-region. However, these approaches only allow for a noise evaluation for the magnitude component, neglecting the impact of noise in the phase. In [4], noise contribution of each measurement channel is also partitioned between two noise sources. Whereas the proposed model of [4] allows complex noise evaluation,

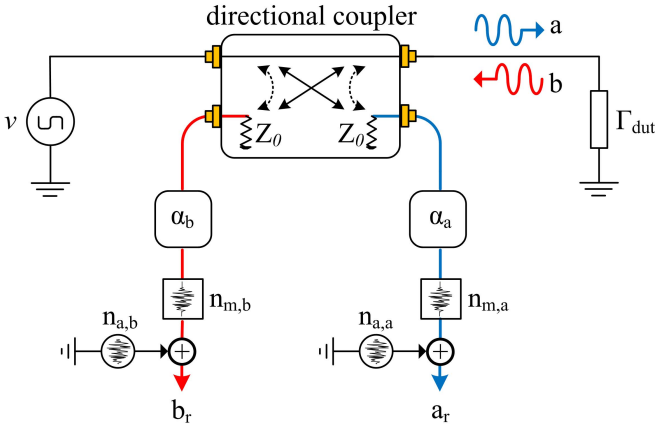

Fig. 2. System-level VNA block diagram for noise behavioral modeling of S-parameter measurements for different DUT reflection coefficients $\boldsymbol{\Gamma}_{\text{dut}}$. Additive and multiplicative noise sources are shown as round and square noise sources, respectively.

the important interdependence between measurement channels of a VNA and their noise sources is not considered. To understand the noise expansion mechanism occurring in VNAs under highly mismatched conditions, the identification and partitioning of all relevant VNA noise sources is required. In addition, understanding interdependence, better known as correlation, between measurement channels and their noise sources is essential to properly describe, and eventually minimize, the noise contributions in measurement of highly mismatched devices.

To analyze the noise contribution on the incident (**a**-wave) and scattered (**b**-wave) traveling waves at the VNA measurement port, a simplified coupler-based VNA block scheme is given in Fig. 2. This configuration is employed for metrology-grade broadband VNAs. Here, the **a**-wave and the **b**-wave are detected by an RF directional-coupler (transmission-line based), and are processed via independent amplification/down-conversion/detection paths. Thus, both waves are subjected to different loss and gain mechanisms due to the presence of components with different performance parameters (i.e., noise figure levels, conversion gain and stability) in both paths. The overall attenuation and delay of these waves is accounted for in the model through the complex transmission coefficients $\boldsymbol{\alpha}_a$ and $\boldsymbol{\alpha}_b$, shown in Fig. 2. The present generation of analog-to-digital converters (ADCs) reaches superior linearity specifications with respect to their predecessors, reducing non-linearity errors to a secondary source of uncertainty in VNA measurements. For this reason, the ADC linearity error is considered negligible in the proposed noise behavioral model. The noise behavior of VNAs employing different **a**-wave and **b**-wave detection schemes can differ from the outlined noise behavioral model.

The overall VNA noise behavior can be partitioned in multiplicative ($\mathbf{n}_m$) and additive ($\mathbf{n}_a$) noise sources [4]. The multiplicative noise accounts for a contribution dependent on the signal level, while the additive noise only depends on the instrument noise floor. Using the VNA noise model shown in Fig. 2, we can derive the noise contribution $\sigma(\boldsymbol{\Gamma}_{\text{dut}})$ for any

given DUT reflection coefficient ($\mathbf{\Gamma}_{\rm dut}$), as follows:

$$\sigma(\Gamma_{\rm dut}) = \frac{\sigma(b_r)}{\sigma(a_r)} = \frac{\Gamma_{\rm dut}\nu\alpha_b n_{m,b} + n_{a,b}}{\nu\alpha_a n_{m,a} + n_{a,a}} \tag{1}$$

where the term $\boldsymbol{\nu}$ denotes the test signal originating from the internal signal source of the VNA.

To parameterize (1) and understand the propagation of various noise sources including their correlations, $\sigma(\mathbf{\Gamma}_{\rm dut})$ and $\sigma(\mathbf{b}_r)$ are evaluated via separate experiments. First, the two noise sources affecting the measurement noise of the $\mathbf{b}_r$-wave are evaluated. The impact of noise floor on the magnitude term $\sigma|\mathbf{b}_r|$ is expected to be most dominant for matched loading conditions (i.e., $|\mathbf{\Gamma}_{\rm dut}| \approx 0$), whereas the signal to noise (SNR) is minimum. Consequently, evaluation of (1) yields the additive noise source $|\mathbf{n}_{a,b}|$ as dominant contributor to the noise floor of the instrument and can be quantified via the measurement of a low-reflection termination (i.e., $|\mathbf{\Gamma}_{\rm dut}| \approx 0$). The $|\mathbf{n}_{a,b}|$ value is equal to the standard deviation in this measurement (line labeled noise floor $|\mathbf{n}_{a,b}|$ in Fig. 3). Unlike [4], where an isolation measurement is used to quantify $|\mathbf{n}_{a,b}|$ value, the proposed method is expected to be more accurate as it more precisely resembles the actual measurement conditions. In addition, the impact of additive noise $|\mathbf{n}_{a,b}|$ on the phase term $\sigma(\angle\mathbf{b}_r)$ is expected to be dominant in matched loading conditions (i.e., $|\mathbf{\Gamma}_{\rm dut}| \approx 0$), and can be evaluated via

$$\sigma(\angle b_r) = \tan^{-1}\left(\frac{|n_{a,b}|}{|\Gamma_{\rm dut}|}\right). \tag{2}$$

See the line labeled (2) in Fig. 3.

The second noise source $|\mathbf{n}_{m,b}|$ affecting the $\mathbf{b}_r$-wave measurement is of multiplicative nature. For accurate estimation of $|\mathbf{n}_{m,b}|$, the influence of $|\mathbf{n}_{a,b}|$ is to be minimized, which is achieved for measurements performed under highly mismatched conditions, as the $\mathbf{b}_r$-wave noise is then predominantly set by $|\mathbf{n}_{m,b}|$. Thus, measurement values acquired for $|\mathbf{\Gamma}_{\rm dut1}| \approx 0.9$ and $|\mathbf{\Gamma}_{\rm dut2}| \approx 0.8$ are used to quantify $|\mathbf{n}_{m,b}|$ using

$$|n_{m,b}| = \frac{\sigma(|\Gamma_{\rm dut1}|) - \sigma(|\Gamma_{\rm dut2}|)}{|\Gamma_{\rm dut1}| - |\Gamma_{\rm dut2}|} \tag{3}$$

where $\sigma|\mathbf{\Gamma}_{\rm dut1}|$ and $\sigma|\mathbf{\Gamma}_{\rm dut2}|$ are determined by calculating the standard deviation of a series of measurement samples acquired for $\mathbf{\Gamma}_{\rm dut1}$ and $\mathbf{\Gamma}_{\rm dut2}$ respectively. The line labeled with (3) in Fig. 3 shows the model result; it can be seen that $\sigma|\mathbf{b}_r|$ is linearly proportional to $\mathbf{\Gamma}_{\rm dut}$ in highly mismatched conditions ($|\mathbf{\Gamma}_{\rm dut}| > 0.1$) and causes expansion of noise in mismatched impedance measurements. This proposed method differs from the classical single-measurement based approach also outlined in [4].

Unlike the magnitude term, the noise from $|\mathbf{n}_{m,b}|$ affecting the phase-term $\sigma(\angle\mathbf{b}_r)$ in mismatched conditions is not proportional to $\mathbf{\Gamma}_{\rm dut}$ and is characterized with the following assumption:

$$\sigma(\angle n_{m,b}) = \sigma(\angle b_r). \tag{4}$$

See the line labeled (4) in Fig. 3.

Second, to support the noise evaluation of RF interferometers, the noise sources affecting the ratio measurements

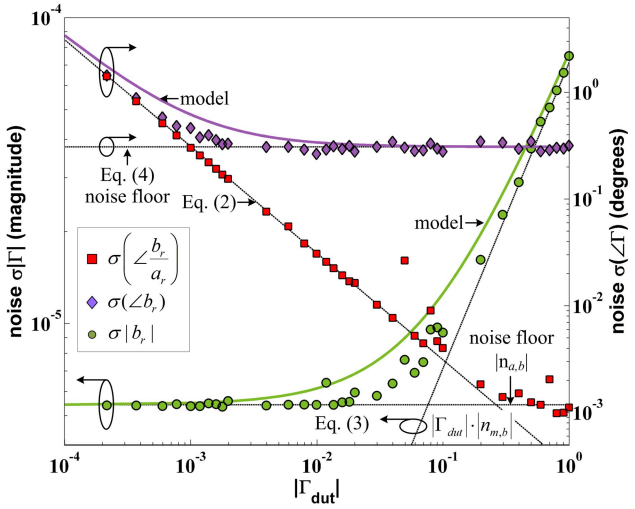

Fig. 3. VNA magnitude and phase noise in $\mathbf{b}_r$-wave and $\mathbf{b}_r/\mathbf{a}_r$ measurements conducted under varying loading conditions $|\mathbf{\Gamma}_{\rm dut}|$. Symbols denote measurement results, whereas the lines represent predictions based on the proposed noise model (see text for further details).

$\mathbf{b}_r/\mathbf{a}_r$ are evaluated where a key element is to understand the correlation between noise sources.

For the $\mathbf{a}_r$-wave, analysis of (1) denominator yields $\mathbf{\Gamma}_{\rm dut}$ insensitive noise behavior. Due to the limited directivity of directional couplers employed in VNAs, the $\mathbf{a}_r$-wave will exhibit second-order sensitivity to $\mathbf{\Gamma}_{\rm dut}$. Nonetheless, the contribution of the additive noise source $|\mathbf{n}_{a,a}|$ is negligible and multiplicative noise $\mathbf{n}_{m,a}$ sets the noise for $\mathbf{a}_r$-wave. Using this, the measurement noise in the magnitude term of $\sigma|\mathbf{b}_r/\mathbf{a}_r|$ is expected to be similar to the noise behavior of $\sigma|\mathbf{b}_r|$. The phase-term measurement noise $\sigma(\angle(\mathbf{b}_r/\mathbf{a}_r))$ is expected to be smaller compared with the $\sigma(\angle\mathbf{b}_r)$ noise, since the noise introduced by the test signal $\boldsymbol{\nu}$ is affecting both the incident $\mathbf{a}_r$-wave and the scattered $\mathbf{b}_r$-wave and, thus, this interdependence is expected to cancel out in $\sigma(\angle(\mathbf{b}_r/\mathbf{a}_r))$. Based on this assumption, the lowest possible noise values for $\sigma(\angle(\mathbf{b}_r/\mathbf{a}_r))$ can be predicted by using (2). The VNA noise model and corresponding parameterization methods are validated via a series of measurements at 3 GHz using a Keysight PNA5225A VNA. The $\mathbf{a}_r$-wave and the $\mathbf{b}_r$-wave are measured over a wide range of $|\mathbf{\Gamma}_{\rm dut}|$ values generated via a 7-mm coaxial mechanical stub-tuner. At each $\mathbf{\Gamma}_{\rm dut}$ value, a total of $20 \cdot 10^3$ measurement points are collected for the $\mathbf{a}_r$-wave and the $\mathbf{b}_r$-wave and the corresponding noise values are subsequently calculated as the standard deviation in the magnitude and phase terms. The results of these measurements are shown with markers in Fig. 3 and agree very well with the model predictions. The measured noise in the magnitude measurements very nicely follows the model predictions given noise floor estimation based on $|\mathbf{n}_{a,b}|$ and (3). It can be seen that $\mathbf{n}_{m,b}$ indeed becomes negligible in matched conditions where $|\mathbf{\Gamma}_{\rm dut}| \approx 0$ and that $|\mathbf{n}_{a,b}|$ sets the noise floor of the instrument up to threshold value of $|\mathbf{\Gamma}_{\rm dut}| \approx 0.1$, according to (1). Beyond this threshold value, $|\mathbf{n}_{m,b}|$ sets the limit for the measurement noise, linearly proportional to $|\mathbf{\Gamma}_{\rm dut}|$, characterized using (3). Similarly, good noise results are achieved for

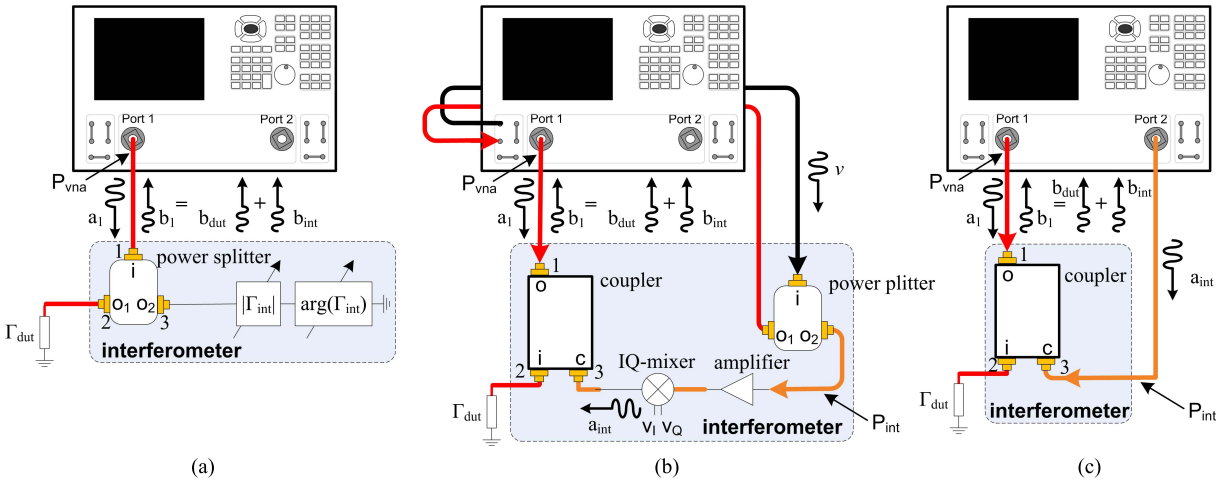

Fig. 4. Schematic representations of three methods for interferometric noise suppression in $\mathbf{\Gamma}$ measurements. (a) Single-source passive method [14]. (b) Single-source active method [15], (c) dual-source active method [16]. Fundamental parts in each interferometer are the 3-port signal combining component and the signal source.

the phase term. The $\mathbf{b}_r$-wave phase noise remains constant for $|\mathbf{\Gamma}_{\rm dut}| > 1 \cdot 10^{-3}$, consistent with the model prediction of (4). For very small $|\mathbf{\Gamma}_{\rm dut}|$ (i.e., $|\mathbf{\Gamma}_{\rm dut}| \approx 0$), the $\mathbf{b}_r$-wave phase-term noise is primarily determined by $|\mathbf{n}_{a,b}|$, consistent with the model prediction of (2). Finally, the measured phase noise in the ratio measurement $\mathbf{b}_r/\mathbf{a}_r$ accurately follows the linear prediction of (2) over three decades in $|\mathbf{\Gamma}_{\rm dut}|$, up to $|\mathbf{\Gamma}_{\rm dut}|$ close to 0.4. As expected, noise introduced by the test signal $\boldsymbol{\nu}$ cancels out in $\sigma(\angle(\mathbf{b}_r/\mathbf{a}_r))$. Furthermore, it is evident the $\sigma(\angle\mathbf{b}_r)$ noise estimated using (4) is predominantly set by test signal $\boldsymbol{\nu}$ noise behavior. For $|\mathbf{\Gamma}_{\rm dut}| > 0.4$, the phase noise in the ratio measurement $\mathbf{b}_r/\mathbf{a}_r$ reaches a minimum noise value and is identified as the noise floor for the phase term.

III. Comparison of Interferometric Techniques

The analysis of the Section II clearly demonstrates, through the noise analysis of (1), that the zero-reflected wave condition provides the smallest noise in S-parameter measurements of a generic DUT. To reach this wave condition, several RF interferometric techniques have been developed [13]–[16] all aiming at cancelling the scattered $\mathbf{b}_{\rm dut}$-wave generated by the (high $|\mathbf{\Gamma}_{\rm dut}|$) DUT through the injection of an additional, compensating the $\mathbf{b}_{\rm int}$-wave signal. Fig. 4 gives a schematic overview of the main approaches presented to date in the literature. To compare the noise-improvement performance of these various interferometric techniques, a generalized flow-graph representation is given in Fig. 5, which includes the required signal combining device to realize the RF interferometer and the relative phase fluctuations between different waves.

With this flow-graph representation both passive ($\mathbf{a}_{\rm int} = 0$) and active interferometers ($\mathbf{a}_{\rm int} \neq 0$) can be analyzed, as well as both classes of passive devices used as signal combining network, i.e., power dividers and transmission line couplers. The VNA is connected to the input of port-1, as shown in Fig. 5. Using classical flow-graph manipulation techniques [21], [22], the $\mathbf{\Gamma}_{\rm vna}$, $\mathbf{\Gamma}_{\rm dut}$, $\mathbf{\Gamma}_{\rm int}$, and the various S-parameters of the combining network can be mutually related to each other, as derived in the Appendix.

The sensitivity equations given in the Appendix are used to analyze passive and active interferometric techniques,

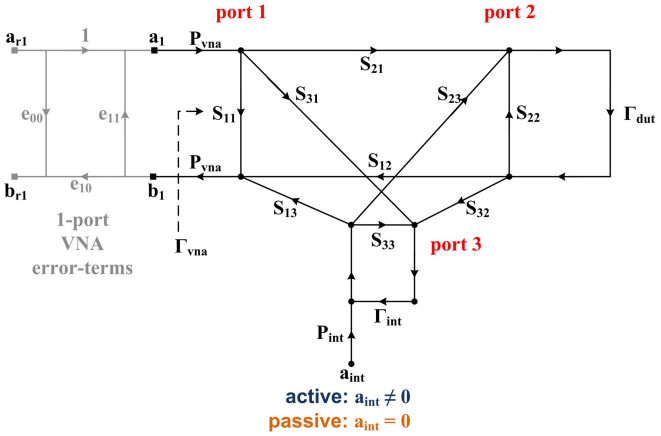

Fig. 5. Flow graph of a one-port VNA with interferometric cancellation of the $\mathbf{b}_1$-wave using a three-port signal-combining device. Port-2 serves as new test port of the VNA and port-3 induces the phase-coherent $\mathbf{a}_{\rm int}$-wave for $\mathbf{b}_1$-wave cancellation.

accounting for the realistic values of the different combining networks employed, i.e., dividers and couplers.

A. Passive Methods

Passive interferometric noise-reduction techniques rely on replicating the scattered $\mathbf{b}$-wave generated by the DUT reflection coefficient through a passive device (i.e., tuner). The parameter $\mathbf{a}_{\rm int}$ in Fig. 5, thus, is zero and $\mathbf{\Gamma}_{\rm int}$ is providing the cancellation condition. In this case, (A2) simplifies to

$$\begin{aligned}\Gamma_{\rm vna} = {} & S_{11}P_{\rm vna}^2 + S_{31}^2 B P_{\rm vna}^2 + S_{21}^2 A P_{\rm vna}^2 + \cdots \\ & \cdots + \left(2\beta\alpha B + S_{31}^2\alpha^2 B^2\right) A P_{\rm vna}^2 + \cdots \\ & \cdots + \left(2\beta\alpha^3 B^2 + S_{21}^2\alpha^2 B\right) A^2 P_{\rm vna}^2\end{aligned}$$

and can be rewritten as

$$\begin{aligned}\Gamma_{\rm vna} = {} & S_{11}P_{\rm vna}^2 + S_{31}^2 B P_{\rm vna}^2 + S_{21}^2 A P_{\rm vna}^2 + \cdots \\ & \cdots + X_1 A P_{\rm vna}^2 + X_2 A^2 P_{\rm vna}^2. \end{aligned} \quad (5)$$

In the cancellation condition (i.e., $\mathbf{b}_1 = 0$) this leads to

$$a_1\left(S_{11} + S_{21}^2 A\right) + \left(X_1 A + X_2 A^2\right) = -a_1 S_{31}^2 B. \quad (6)$$

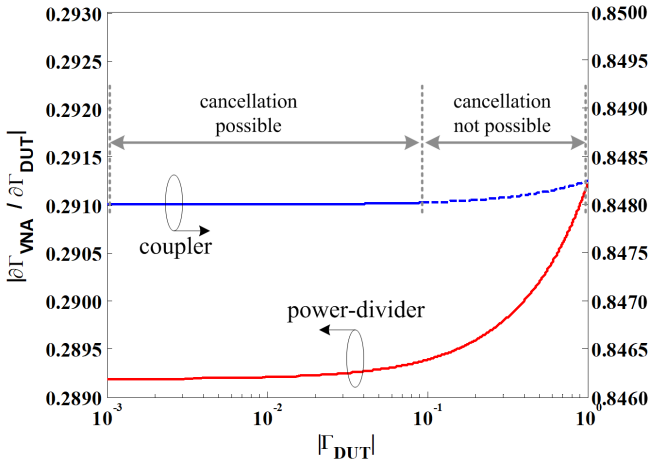

Fig. 6. Simulation results for two different implementations of the three-port signal-combining device used in passive interferometers, showing the sensitivity of the input reflection coefficient measured with the VNA ($\mathbf{\Gamma}_{\rm vna}$) to variations in device reflection coefficient at the measurement port of the interferometer ($\mathbf{\Gamma}_{\rm dut}$).

From the evaluation of (A3), it is evident that the sensitivity ratio ($\partial\mathbf{\Gamma}_{\rm vna}/\partial\mathbf{\Gamma}_{\rm dut}$) cannot exceed 1 for passive techniques due to transmission path losses. Furthermore, realizing high sensitivity for $\partial\mathbf{\Gamma}_{\rm dut}$ requires transmission losses $\mathbf{S}_{21}$ to be minimal, see (5) and (6). In addition, the losses between the input and both output ports of the passive device need to be comparable ($\mathbf{S}_{21} \approx \mathbf{S}_{31}$), due to the limited magnitude of the reflection coefficient that can be provided (i.e., $|\mathbf{\Gamma}_{\rm int}| < 1$) for cancellation. For this reason, it is not possible to use a broadband directional coupler to realize passive cancellation for DUTs presenting a $|\mathbf{\Gamma}_{\rm dut}|$ higher than 0.1 due to the large difference between transmission and coupling losses, i.e., $\mathbf{S}_{21} \gg \mathbf{S}_{31}$. The dual condition is not considered ($\mathbf{S}_{21} \ll \mathbf{S}_{31}$), as this would provide very low sensitivity ($\partial\mathbf{\Gamma}_{\rm vna}/\partial\mathbf{\Gamma}_{\rm dut}$). This effect is shown by using parameters of commercially available directional couplers in calculating (A3) with the results shown in Fig. 6. It is evident that cancellation is only possible for $\mathbf{\Gamma}_{\rm dut}$ up to 0.1 (solid line), while the remaining $\mathbf{\Gamma}_{\rm dut}$-region (dotted line) is not reachable due to the passive nature of the tuner. Due to this constraint, most passive RF interferometers use power dividers, e.g., a Wilkinson power divider [14], see Fig. 4(a).

For accurate measurements over the entire range of $\mathbf{\Gamma}_{\rm dut}$ values, the measurement resolution has to be constant. However, a non-zero $\mathbf{X}_1$ and $\mathbf{X}_2$ in (6) leads to unwanted $\mathbf{\Gamma}_{\rm dut}$ and $\mathbf{\Gamma}_{\rm int}$ dependent cross leakage, limiting the sensitivity. Hence, $\boldsymbol{\alpha}$ remains a critical parameter of the 3-port combining devices used in passive interferometers. To investigate the impact of $\boldsymbol{\alpha}$ on the measurement sensitivity, parameters of a commercially available power divider are used for calculation of (A3) with the results shown in Fig. 6. Clearly, the power-divider approach suffers more from the unwanted crosstalk between the two combining ports ($\boldsymbol{\alpha}$), reducing the measurement resolution. However, unlike the directional coupler, the power divider can achieve cancellation for the entire range of $\mathbf{\Gamma}_{\rm dut}$ values.

B. Active Methods

Active interferometric noise suppression is realized via the injection of an $\mathbf{a}_{\rm int}$-wave (see Fig. 5) generated by employing active components. This can be either an IQ-steering technique [15] shown in Fig. 4(b) or a second, phase coherent, source [16] as shown in Fig. 4(c). Hence, active techniques are not limited to the constraint of $\mathbf{S}_{21} \approx \mathbf{S}_{31}$, required by passive ones, thus employ coupled line coupler as the combining device due to the reduced $\boldsymbol{\alpha}$, as shown in Fig. 6. If we include the effect of the relative (phase) fluctuations between the signals $\mathbf{a}_1$ and $\mathbf{a}_{\rm int}$ in (A2) and those arising from the different propagation paths, equation becomes

$$\begin{aligned} b_1 = {} & a_1\big(S_{11} + S_{21}^2 A + S_{31}^2 B + 2\beta\alpha BA + S_{31}^2\alpha^2 B^2 A + \cdots \\ & \cdots + 2\beta\alpha^3 B^2 A^2 + S_{21}^2\alpha^2 BA^2\big)P_{\rm vna}^2 + \cdots \\ & a_{\rm int}\big(S_{13} + S_{12}\alpha A + S_{13}\alpha^2 BA + S_{12}\alpha^3 BA^2 + \cdots \\ & \cdots + S_{13}\alpha^4 B^2 A^2\big)P_{\rm int}P_{\rm vna}. \end{aligned}$$

This can be rewritten as

$$b_1 = a_1 K P_{\rm vna}^2 + a_{\rm int} L P_{\rm int} P_{\rm vna}. \tag{7}$$

1) Single- and Dual-Source Interferometers: Single-source interferometers have one signal source $\boldsymbol{\nu}$ that generates $\mathbf{a}_1$ and $\mathbf{a}_{\rm int}$ signals [15], see Fig. 4(b). The relation between $\boldsymbol{\nu}$ and both signals can be expressed as follows:

$$\begin{aligned} a_1 &= \nu P_{\rm vna}^* \\ a_{\rm int} &= \nu G_{\rm int} P_{\rm vna}^*. \end{aligned} \tag{8}$$

Here, $\mathbf{G}_{\rm int}$ is the active gain needed to compensate for the various losses introduced by the couplers, cables, and passive IQ-mixers. Furthermore, $\mathbf{P}_{\rm vna}$ and $\mathbf{P}_{\rm vna}^*$ present two distinct parts of the $\mathbf{a}_1$-wave signal path, where $\mathbf{P}_{\rm vna}^*$ is also shared by the $\mathbf{a}_{\rm int}$-wave signal. This single-source method is realized by splitting the $\boldsymbol{\nu}$ signal before measurement of the $\mathbf{a}_1$-wave and the $\mathbf{b}_1$-wave signals, see Fig. 4(b). The disadvantage of this method is that it suffers from separate routing of $\mathbf{a}_1$ and $\mathbf{a}_{\rm int}$ signals, requiring the use of lengthy cables, denoted with $\mathbf{P}_{\rm vna}$, $\mathbf{P}_{\rm vna}^*$, and $\mathbf{P}_{\rm int}$ in Fig. 4(b). Since the noise and drift effects of the VNA test-port cables can be much larger than the VNA noise [23], the stability of both cables significantly limits the performance of this approach. For single-source based cancellation ($\mathbf{b}_1 = 0$), (7) can be expressed as

$$\nu K P_{\rm vna}^2 P_{\rm vna}^* = \nu G_{\rm int} L P_{\rm int} P_{\rm vna} P_{\rm vna}^*. \tag{9}$$

In (9), the left side of the equations represents the scattered wave generated by $\mathbf{\Gamma}_{\rm dut}$, whereas the right side of the equation represents the scattered wave generated by the interferometer. From (9), it is evident that the cancellation condition is insensitive to variations in the $\boldsymbol{\nu}$ source. However, as both scattered waves travel through independent paths, the cancellation condition is also sensitive to unwanted instability effects originating from the use of two different cable paths $\mathbf{P}_{\rm vna}$, $\mathbf{P}_{\rm vna}^*$, and $\mathbf{P}_{\rm int}$, respectively.

A similar analysis can be applied to evaluate dual-source interferometer [16], where two separate signal sources are used

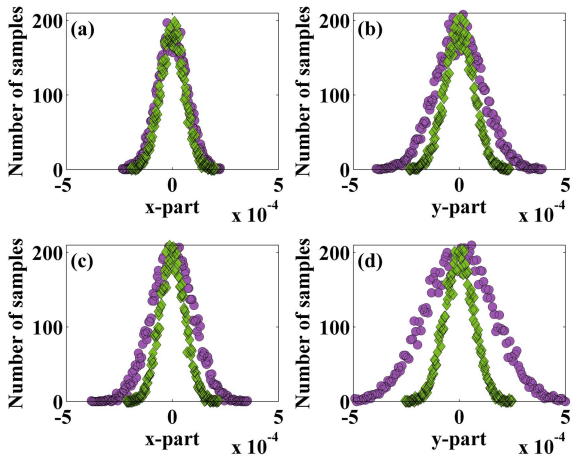

Fig. 7. Monte Carlo noise simulation results for two active interferometric techniques, detailing **b**-wave cancellation sensitivity for single-source (green diamonds) and dual-source (purple circles) interferometers. (a) and (b) Complex **b**-wave cancellation discrepancies caused by variations of cable parameters are shown. (c) and (d) **b**-wave complex cancellation discrepancies caused by variations of cable and source parameters.

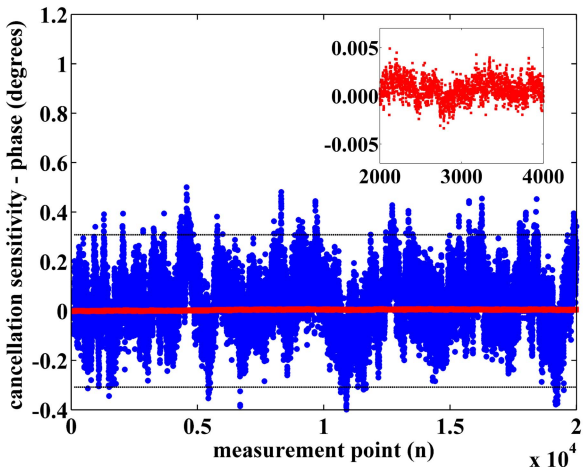

Fig. 8. Measurement results showing the cancellation sensitivity for the phase-component realized with two active interferometer topologies at 3 GHz. Blue circles: dual-source. Red squares: single-source (inset). Black line: phase-component stability of **b**-wave measured using method outlined in (4).

to generate $\mathbf{a}_1$ and $\mathbf{a}_{\text{int}}$, see Fig. 4(c). Hence, for cancellation ($\mathbf{b}_1 = 0$), (7) now becomes

$$a_1 K P_{\text{vna}}^2 = -a_{\text{int}} L P_{\text{int}} P_{\text{vna}}. \tag{10}$$

This approach also suffers from the use of lengthy cables as separate routing of the $\mathbf{a}_1$ and $\mathbf{a}_{\text{int}}$ signals is unavoidable. An additional problem with respect to the single-source method is uncorrelated noise and drift effects originating from the different signal sources.

2) Simulation Evaluation: To validate the **b**-wave cancellation capabilities of both the active interferometric methods, (9) and (10) are evaluated via Monte Carlo simulations conducted in Advanced Design System software. To investigate the effect of non-ideal cables and signal sources, parameter variations are assigned to the magnitude and phase components of cable paths and signal sources. The variations in cable parameters are based on an evaluation technique outlined in [23]: the magnitudes of $\mathbf{P}_{\text{vna}}$, $\mathbf{P}_{\text{int}}$, $\mathbf{a}_1$, and $\mathbf{a}_{\text{int}}$ are varied by 0.01% and their corresponding phases are varied by 0.2deg (both Gaussian distributions).

For the single-source interferometer, the cancellation sensitivity of (9) is investigated by propagating variations assigned to $\mathbf{P}_{\text{vna}}$ combined with $\mathbf{P}_{\text{vna}}^*$, $\mathbf{P}_{\text{int}}$, and $\mathbf{a}_1$. For the dual-source method, the cancellation sensitivity is investigated by (10) via propagating variations assigned to $\mathbf{P}_{\text{vna}}$, $\mathbf{P}_{\text{int}}$, $\mathbf{a}_1$, and $\mathbf{a}_{\text{int}}$. The results are shown in Fig. 7.

In Fig. 7(a) and (b), the complex **b**-wave cancellation discrepancies caused by propagation of cable parameter variations are shown. The simulation results show that the single-source method has slightly lower noise compared with the dual-source technique. The reason that the single-source method of Fig. 4(b) has marginally better noise than the dual-source method of Fig. 4(c) is the shared cable $\mathbf{P}_{\text{vna}}^*$ path in the single-source configuration.

The **b**-wave cancellation discrepancies shown in Fig. 7(c) and (d) are predominantly noticeable, when propagating $\mathbf{a}_1$ and $\mathbf{a}_{\text{int}}$ signal parameter variations combined with cable parameter variations. As expected, the **b**-wave cancellation condition for single-source configuration is insensitive to $\mathbf{a}_1$ and $\mathbf{a}_{\text{int}}$ signal parameter variations originating from $\boldsymbol{\nu}$.

C. Measurement Comparison

As a further evaluation of the two active interferometer types, a measurement of single- and dual-source interferometers was carried out using a four-port Keysight PNA-X (PNA5257A). This VNA has two signal sources and allows individual control of magnitude and phase components. First, stability between both signal sources used by dual-source interferometer is evaluated. Like [16], port-1 and port-3 of the VNA provide $\mathbf{a}_1$ and $\mathbf{a}_{\text{int}}$ signals, with amplitude and phase control of each signal source available through the firmware (option: 080) of the PNA-X. Both signals are subsequently measured by the receivers of port-2 and port-4. Subsequently, the stability between $\mathbf{a}_1$ and $\mathbf{a}_{\text{int}}$ signals in single-source interferometer is evaluated using port-1 of the VNA to provide the $\mathbf{a}_1$ signal source and to serve as input for the single-source interferometer as shown in Fig. 4(b). Again, both signals are subsequently measured by the receivers of port-2 and port-4.

In both experiments, the power level of each signal source is set to -10 dBm, and subsequently, $20 \cdot 10^3$ measurement values are extracted at 3 GHz from both the receivers (port-2 and port-4). From these values, the ratio $\mathbf{a}_{\text{int}}/\mathbf{a}_1$ is calculated and normalized to demonstrate the stability between the two signals.

The linear magnitude stability of $\mathbf{a}_{\text{int}}/\mathbf{a}_1$ for both methods is found to be comparable and smaller than $1 \cdot 10^{-4}$. The result of the relative phase stability between $\mathbf{a}_1$ and $\mathbf{a}_{\text{int}}$ signals is shown in Fig. 8. As expected, these results demonstrate the much higher phase stability of the single-source configuration compared with the dual-source method [16]. Moreover, as shown in Fig. 8, the model predictions, plotted as black dashed line, accurately correlate with the experimentally found phase fluctuations for the dual-source method.

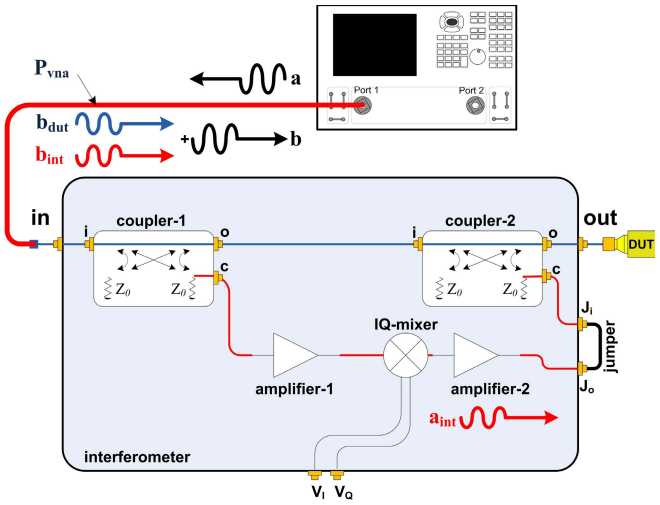

Fig. 9. Block-diagram of the new HF interferometer utilizing IQ-mixer steering technique for IQ-modulation of the $\mathbf{a}_{\text{int}}$-wave in order to achieve optimal cancellation of the reflected $\mathbf{b}_{\text{dut}}$-wave for all $\boldsymbol{\Gamma}_{\text{dut}}$ values.

IV. Novel Single-Source Interferometer Module

Based on the analyses of the previous chapters, a new RF interferometer is designed. An active interferometer approach was chosen in order not to be limited in performance and $\boldsymbol{\Gamma}$ range as shown in Fig. 6 for passive interferometers. Based on the results shown in Figs. 7 and 8, the new interferometer has been filed for patent [17] and is based on a single source concept. Two major improvements were made with respect to the approach given in Fig. 4(b), in order to remove the effect of the cable $\mathbf{P}_{\text{int}}$ and in order not to be limited to application to VNAs with front panel jumpers. A simplified block diagram of the new interferometer architecture is shown in Fig. 9. The interferometer generates a phase coherent $\mathbf{a}_{\text{int}}$-wave using the $\mathbf{a}_1$ signal generated by the VNA. The entire interferometer is confined in the test path of the measurement system, as a single add-on module. A distinct advantage of the new design is the exclusion of separate lengthy cables between the drive ($\mathbf{a}_1$) and the interferometer path ($\mathbf{a}_{\text{int}}$) that significantly reduces independent cable error contributions.

A directional coupler (coupler-1) is used to couple a portion of the $\mathbf{a}_1$ wave signal into the IQ-path. The through path formed between port-in and port-out of the interferometer, comprising of coupler-1 and coupler-2, forms the measurement path of the VNA. This approach offers a sensitivity advantage compared with the power divider approach [14], as it achieves higher measurement resolution due to its reduced losses. The coupled wave at port-c of coupler-1 is used to generate a phase-coherent wave $\mathbf{a}_{\text{int}}$. A broadband amplifier (amplifier-1) ensures a sufficient power level to drive the LO-port of the IQ-mixer. A second amplifier (amplifier-2) compensates for the additional losses introduced by coupler-2 and the conversion loss of the IQ-mixer. The IQ-ports of the mixer are controlled with dc in-phase (V_I) and quadrature-phase (V_Q) voltages to control both the magnitude and phase of the $\mathbf{a}_{\text{int}}$-wave. The interferometer path in the new design excludes the use of lengthy cables, hence applying $\mathbf{P}_{\text{int}} = 1$ to (9) leads

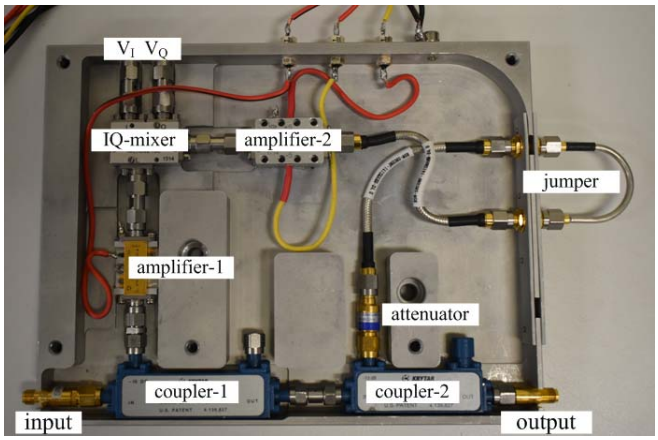

Fig. 10. HF interferometer module designed for the 2–18 GHz frequency range. The use of a passive IQ-mixer requires two additional amplifiers to compensate for losses.

to the following cancellation condition ($\mathbf{b}_1 = 0$):

$$a_1 K P_{\text{vna}}^2 = -a_1 G_{\text{int}} L P_{\text{vna}}^2. \tag{11}$$

This shows that the sensitivity of the new interferometer is only limited by cable fluctuations in the $\mathbf{P}_{\text{vna}}$ path.

Two interferometers are designed to cover the complete frequency band of 1–18 GHz. Fig. 10 gives a top-view photograph of the HF interferometer, operating from 2 up to 18 GHz, whereas the low-frequency (LF) interferometer is designed for operation from 1 up to 5 GHz.

The noise performance of the interferometer is determined by three sources of uncertainty, noise performance of the **a**-wave signal used to drive the IQ-mixer, noise performance of both amplifiers use to increase the signal power level and the spectral purity of both V_I and V_Q dc voltages used to drive the IQ-ports of the mixer.

In the design of both interferometer modules, low-noise amplifiers are used to retain low-noise figure for the modules. The V_I and V_Q dc voltages are generated with low-noise 24-bit digital-to-analog convertors by National Instruments. To enhance the spectral purity of both signals, low-pass filters are mounted at the input of IQ-ports of the mixer. Thermal stability of all components is crucial to reduce drifting error. Hence, both interferometers are mounted in a dedicated housing unit for improved thermal stability, with precision 3.5-mm connectors at their input and output ports.

V. Measurement Experiments and Discussion

In this section, the performance of VNA systems employing the novel interferometer is benchmarked in two experiments versus traditional 50-Ω VNA S-parameter measurements. First, broadband measurements of highly mismatched planar impedances are carried out to identify the increased impedance resolution achievable with the new add-on interferometer. Second, an SMM setup is conceived to demonstrate, quantitatively, the spatial resolution enhancement achievable with the interferometer.

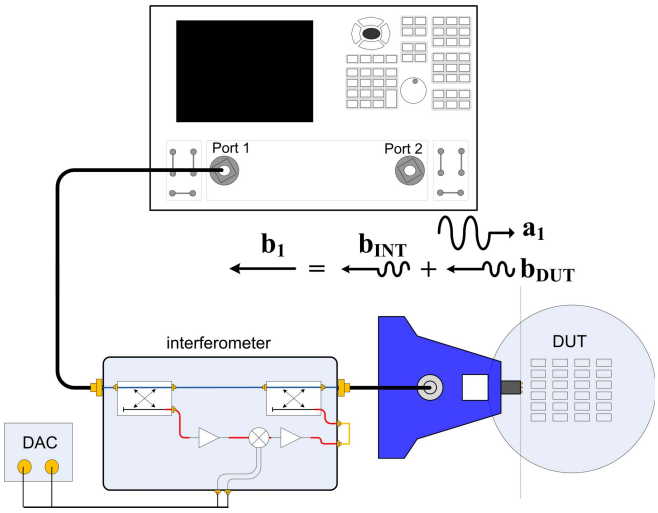

Fig. 11. Block diagram of the novel interferometer-based VNA for broadband measurement of highly mismatched CPW devices.

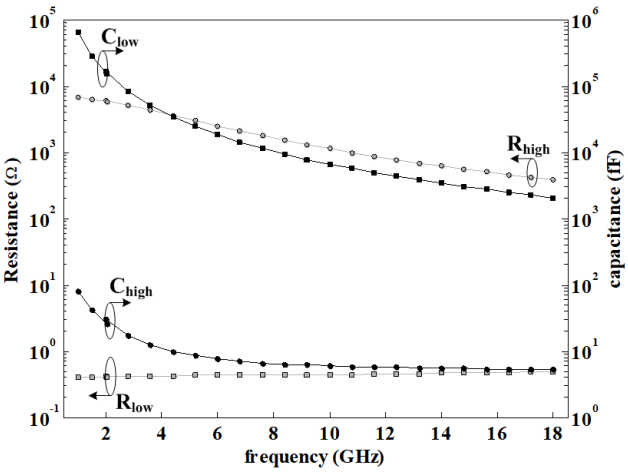

Fig. 13. Measurement results of CPW $\mathbf{Z}_{low}$ and $\mathbf{Z}_{high}$ impedance standards in the 1–18 GHz frequency range, with resistance R_{low} and R_{high} and stray capacitance C_{low} and C_{high} values corresponding to the CPW standards.

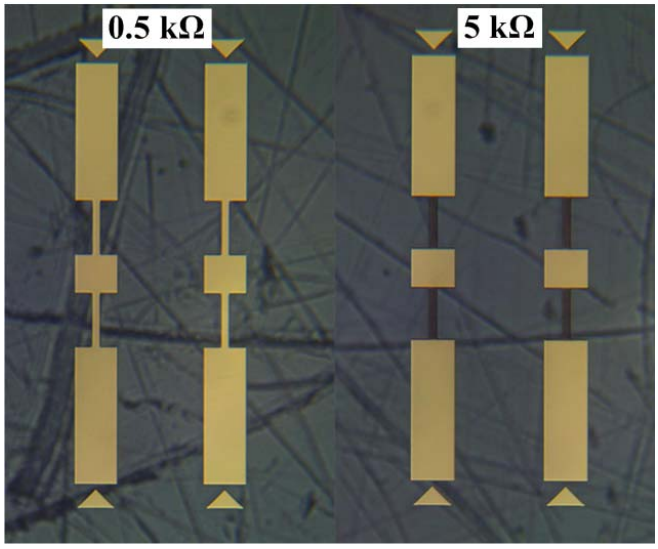

Fig. 12. Photograph of 0.5-Ω and 5-kΩ CPW impedance standards manufactured on a fused-silica substrate, using a dedicated aluminum on titanium process developed at the Delft University of Technology [24], [25].

A. Broadband Planar Measurements

Fig. 11 shows a sketch of the system for broadband measurements of extreme-impedance co-planar waveguide (CPW) devices. Both the LF- and HF-interferometers are employed to cover the frequency range from 1 up to 18 GHz. A Keysight PNA (5225A) is used for input reflection coefficient $\mathbf{\Gamma}$ measurements at a test-port power level of -5 dBm and IF-bandwidth of 30 Hz. At the output port of the interferometer, a GSG infinity probe with 150-μm pitch size is connected.

A set of mismatched CPW impedance standards are manufactured to experimentally demonstrate the active noise suppression in highly mismatched loading conditions. A photograph of both impedance standards is shown in Fig. 12. The impedance standards are designed with nominal impedance of 0.5 Ω ($\mathbf{Z}_{low}$) and 5 kΩ ($\mathbf{Z}_{high}$) [24], [25].

The VNA sequentially utilizes the novel LF- and HF-interferometers to measure the S-parameters of both CPW impedance standards. To benchmark the interferometer-based VNA results to conventional VNA performance, the interferometer first is deactivated and the measurement system is calibrated using the well-known SOL technique utilizing a 50-Ω reference impedance, a short and an open standard. After completion of the calibration process, the $\mathbf{Z}_{low}$ and $\mathbf{Z}_{high}$ impedance standards are measured.

The resistance R_{low} and R_{high} and the stray capacitance C_{low} and C_{high} corresponding to $\mathbf{Z}_{low}$ and $\mathbf{Z}_{high}$ standards are shown in Fig. 13. In addition, a total of 101 sweeps are conducted to collect sufficient measurement values to estimate the corresponding noise values, see Fig. 14(a) and (b). Subsequently, both impedance standards are remeasured with the interferometer activated. The $\mathbf{b}_r$-wave is cancelled for each frequency point by IQ-modulation of $\mathbf{a}_{int}$-wave with IQ-mixer steering technique described in [15] in combination with minimization algorithm based on a Newton–Raphson [26] method. After completion of the minimization step, the V_I and V_Q values are stored for each frequency point. For all subsequent measurements, the software automatically sets these V_I and V_Q values corresponding to the frequency until all frequency points of the sweep are measured. Again, in total 101 sweeps are conducted to collect enough measurement values to estimate the noise of the interferometer. The resulting noise values for R_{high} and C_{high} are shown in Fig. 14(a) and for R_{low} and C_{low} in Fig. 14(b), respectively, for both the LF- and HF-interferometer. The $\mathbf{Z}_{low}$ results shown in Fig. 14(b) demonstrate marginal noise improvement of the interferometer-based VNA with respect to the conventional VNA. This likely is caused by the susceptibility of low-ohmic device measurements ($\mathbf{Z}_{dut} < 1$ Ω) to instabilities in contact resistance between the probe and DUT. In contrast, the $\mathbf{Z}_{high}$ results of Fig. 14(a) demonstrate a significant noise improvement over the entire frequency range, ranging from a factor 8 at 1 GHz up to a factor 20 at 18 GHz.

The frequency dependence in the noise improvement results of Fig. 14 is caused by a combination of various effects. First, the devices used in the interferometer modules exhibit strong

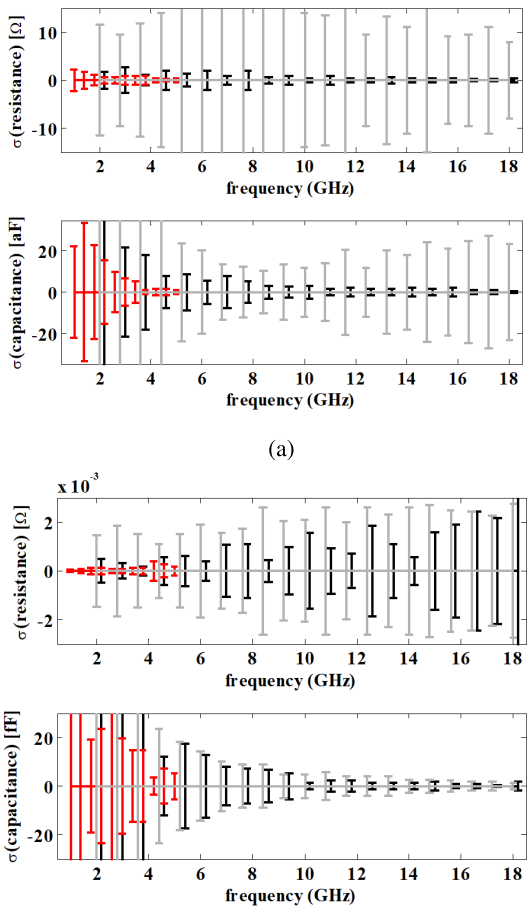

Fig. 14. Measurement noise results corresponding to CPW $\mathbf{Z}_{\text{low}}$ and $\mathbf{Z}_{\text{high}}$ impedance standards in the 1–18 GHz frequency range. (a) Measurement noise values for the $\mathbf{Z}_{\text{high}}$ impedance standard. (b) Results of $\mathbf{Z}_{\text{low}}$ impedance standard. Gray bars denote noise values measured with a conventional VNA; red and black bars show noise values for a VNA with the novel LF- and HF-interferometer, respectively.

frequency dependence in their electrical performance which is difficult to compensate completely. Especially, high coupling losses at lower frequencies are expected to strongly contribute to the less favorable noise improvement for C_{high} and C_{low} at low frequencies.

The second effect is believed to be unwanted leakage of the $\mathbf{a}_{\text{int}}$ signal from the coupled port to the output port of directional coupler-2 of the interferometer module (Fig. 9). This unwanted leakage signal causes standing waves, which in turn leads to degradation of the phase performance of the cancelled **b**-wave. The directivity of the broadband transmission-line-based directional coupler improves with frequency, resulting in improved noise behavior for capacitance measurements at higher frequencies.

The third effect origins from the complex nature of the $\mathbf{Z}_{\text{low}}$ and $\mathbf{Z}_{\text{high}}$ standards. The C_{high} and C_{low} values exhibit a strong frequency dependence, changing more than three orders of magnitude in nominal value from 1 to 18 GHz. Over this same frequency range, the R_{low} and R_{high} values only change less than a factor 10, leading to less frequency dependence in the noise performance.

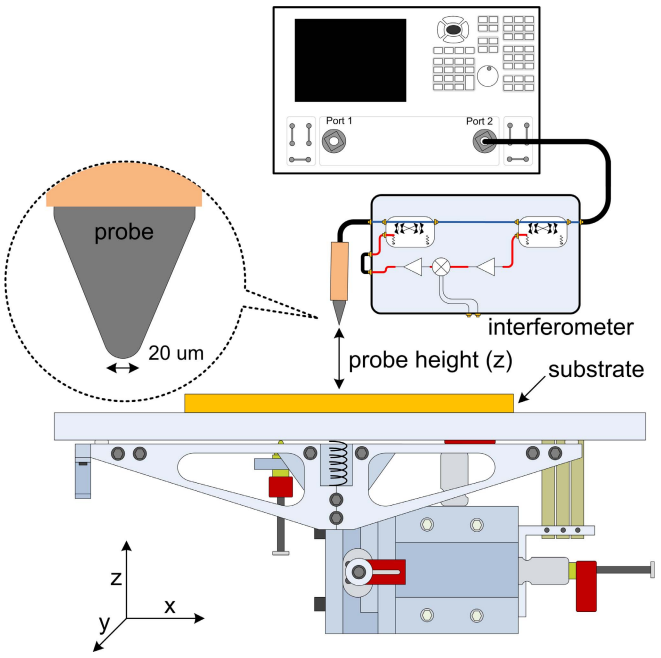

Fig. 15. Schematic block diagram of the SMM employing the novel LF-interferometer to improve the measurement resolution of the system.

B. Spatial Resolution of Scanning Microwave Microscope

Fig. 15 gives a sketch of the conceived SMM setup, equipped with the LF interferometer. The localized input reflection coefficient ($\mathbf{\Gamma}$) is acquired using a Keysight PNA (5225A) at a test-port power level of -7 dBm and IF bandwidth of 30 Hz. A coaxial probe with circa 20 μm tip radius is used as the SMM sensing element. To maintain long-term stability, the entire probe fixture is rigidly fixed and the sample under test (SUT) is mounted on a xyz-stage, offering computer numerical control motor resolution of 30 nm in each axis. The entire measurement setup is built on an active-air supported vibration isolation table suitable for nanoscale measurements. Measurements are conducted at 4 GHz with the environmental temperature in the laboratory at (23 $\pm$ 0.1) °C.

First, the spatial resolution of the SMM system without interferometer is evaluated by measuring the $\mathbf{\Gamma}$-to-height sensitivity function $\mathbf{H}_{\text{off}}$ of the SMM. A fused silica wafer is mounted on the xyz-stage and consecutively positioned in close vicinity to the probe tip (nominal position). Subsequently, the xyz-stage is used to introduce height steps of 1 μm (downward in z-axis) until a 100-μm distance from the nominal position is reached. At each step, $\mathbf{\Gamma}_{\text{off}}$ is measured with the VNA by acquiring 101 values to determine also the noise $\sigma(\mathbf{\Gamma}_{\text{off}})$. These $\mathbf{\Gamma}_{\text{off}}$ results with corresponding noise values $\sigma(\mathbf{\Gamma}_{\text{off}})$ are shown in Fig. 16. In the next step of the experiment, the interferometer is switched ON. With the substrate positioned at the nominal position, the interferometer is now employed to minimize the reflection coefficient to the target value $\mathbf{\Gamma} < -80$ dB.

These interferometer settings (V_I and V_Q) are maintained constant for all subsequent measurements, with the xyz-stage introducing height steps of 1 μm (downward in z-axis) until again a 100 μm distance is reached. The results of $\mathbf{\Gamma}_{\text{on}}$ measured with the interferometer-based VNA and the

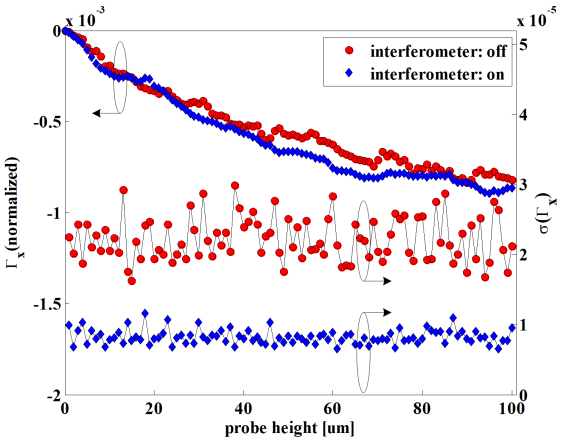

(a)

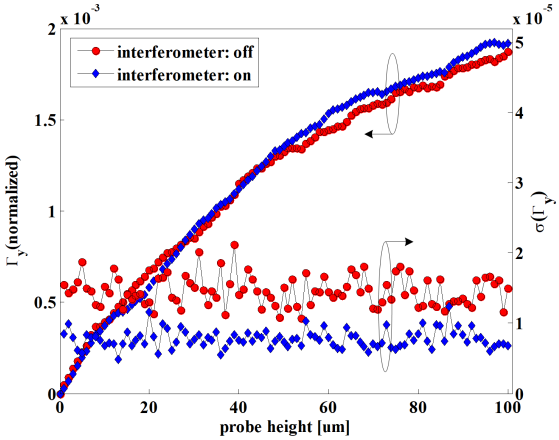

(b)

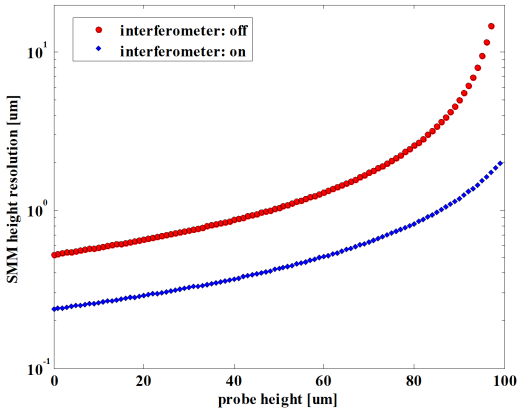

(c)

Fig. 16. Sensitivity curves **H** and corresponding measurement noise value $\sigma(\mathbf{\Gamma})$ for the SMM system. (a) Real-parameter and (b) imaginary-parameter of the sensitivity-curve. (c) Height-dependent spatial resolution of the SMM system.

corresponding noise $\sigma(\mathbf{\Gamma}_{\text{on}})$ are shown in Fig. 16. The $\mathbf{\Gamma}$ curves for both experiments given in Fig. 16(a) and (b) are very close to each other, as the interferometer does not change the physical interaction between the probe tip and SUT. From the $\mathbf{\Gamma}$ measurements as function of probe height z, the **H**-function can be determined via

$$H = \frac{\partial \Gamma}{\partial z}. \tag{12}$$

The spatial resolution of the SMM system is directly related to the measurement noise $\sigma(\mathbf{\Gamma})$ and **H**

$$u_{\text{height}} = \frac{\sigma(\Gamma)}{H}. \tag{13}$$

It is evident from Fig. 16 that the imaginary part of the reflection coefficient ($\mathbf{\Gamma}_y$) exhibits higher sensitivity to probe height in comparison with the real part of $\mathbf{\Gamma}$. Therefore, $\mathbf{\Gamma}_y$ is used to estimate H as well as the spatial sensitivity of the SMM system, as this provides the highest resolution. In Fig. 16(c), the resulting spatial sensitivity values are shown for the SMM with and without interferometer. The SMM resolution is strongly correlated with the probe height and exhibits the highest sensitivity in close vicinity of the SUT. The best sensitivity for the SMM system without interferometer is 450 nm; adding the interferometer enhances the sensitivity with almost a factor 2 down to 240 nm.

VI. Conclusion

A method is presented for evaluation of the measurement noise in S-parameter measurements as a function of device impedance. The modeling techniques utilize two localized noise sources approach [4] to accurately replicate the noise behavior of each measurement channel in a VNA under dynamic loading conditions. The proposed method allows evaluation of correlations between the **a**-wave and the **b**-wave measurement channels, their corresponding sources of noise and their influence on both magnitude and phase components, a distinct advantage compared with previous work. The validity of the proposed method is proven via excellent agreement of its predictions with measurements over a wide range of $\mathbf{\Gamma}$-loading conditions.

Using the proposed noise evaluation method, several existing VNA interferometric techniques are compared for their capability to suppress the measurement noise in highly mismatched conditions. The analysis shows that the 3-port signal combining components, signal sources and cables are critical parts in the cancellation sensitivity of present interferometers. Passive interferometers present clear limitations in coverage of $\mathbf{\Gamma}_{\text{dut}}$ range and measurement sensitivity. The cancellation sensitivity of single-source and dual-source active interferometers appears sensitive to unavoidable cable errors. Simulations and measurements show that the dual-source interferometers in addition suffer from source instabilities.

Based on these findings, a new single-source interferometer is designed that excels in phase stability due to reduced use of cables. The implementation as a single add-on unit allows the interferometer to be used in combination with any VNA, also in multi-port configuration. Two versions were built, one operating in the 1–5 GHz range and the second in the 2–18 GHz range. The new interferometer allows for unique, real-time broadband cancellation during a VNA frequency sweep, with no measurement overhead time compared with conventional 50-Ω VNA measurements. Two experiments demonstrate the advantages and the quality of the new RF interferometer. Broadband planar measurements of a set of highly mismatched CPW impedances demonstrate a factor 20 noise reduction in the measurement of a 5-kΩ impedance at 18 GHz. Application of the interferometer in a SMM system enhances the height resolution with a factor 2 down to 240 nm.

In conclusion, this paper provides quantifiable modeling and measurement data of a true interferometer-based VNA achieving a substantial reduction in noise uncertainty (up to a factor 20 at 18 GHz) in impedance measurements under highly mismatched conditions over the complete 1–18 GHz frequency range.

APPENDIX

The S-parameters of the combining network given in Fig. 5 can be linked via

$$\begin{aligned}\Gamma_{\text{vna}} &= \frac{b_1}{a_1} \\ &= P_{\text{vna}}^2\Bigg(S_{11} + S_{21}^2\sum_{n=1}^{\infty}\alpha^{2(n-1)}A^nB^{n-1} + \cdots \\ &\qquad \cdots + 2\beta\sum_{n=1}^{\infty}\alpha^{2n-1}A^nB^n \\ &\qquad + S_{31}^2\sum_{n=1}^{\infty}\alpha^{2(n-1)}A^{n-1}B^n\Bigg) + \cdots\cdots \\ &\quad + \frac{a_{\text{int}}}{a_1}P_{\text{int}}P_{\text{vna}}\Bigg(S_{13} + S_{12}\sum_{n=1}^{\infty}\alpha^{2n-1}A^nB^{n-1} \\ &\qquad + \cdots\cdots + S_{13}\sum_{n=1}^{\infty}\alpha^{2n}A^nB^n\Bigg)\end{aligned} \tag{A1}$$

with

$$A = \frac{\Gamma_{\text{dut}}}{1 - S_{22}\Gamma_{\text{dut}}} \qquad B = \frac{\Gamma_{\text{int}}}{1 - S_{22}\Gamma_{\text{int}}}.$$

If we furthermore assume that

$$n = 2, \quad S_{i,j} = S_{j,i}, \quad \alpha = S_{23} = S_{32}, \quad \beta = S_{21}S_{13} = S_{31}S_{12}$$

(A1) can be expressed as follows:

$$\begin{aligned}\Gamma_{\text{vna}} &= S_{11}P_{\text{vna}}^2 + S_{31}^2BP_{\text{vna}}^2 + S_{13}\frac{a_{\text{int}}}{a_1}P_{\text{int}}P_{\text{vna}} + \cdots \\ &\quad \cdots + A\Bigg(S_{12}\alpha\frac{a_{\text{int}}}{a_1}P_{\text{int}}P_{\text{vna}} + 2\beta\alpha BP_{\text{vna}}^2 + S_{21}^2P_{\text{vna}}^2 \\ &\qquad + \cdots\cdots + S_{31}^2\alpha^2B^2P_{\text{vna}}^2 \\ &\qquad + S_{13}\alpha^2B\frac{a_{\text{int}}}{a_1}P_{\text{int}}P_{\text{vna}}\Bigg) \\ &\quad + \cdots\cdots + A^2\Bigg(2\beta\alpha^3B^2P_{\text{vna}}^2 + S_{21}^2\alpha^2BP_{\text{vna}}^2 + \cdots \\ &\qquad \cdots + S_{12}\alpha^3B\frac{a_{\text{int}}}{a_1}P_{\text{int}}P_{\text{vna}} \\ &\qquad + S_{13}\alpha^4B^2\frac{a_{\text{int}}}{a_1}P_{\text{int}}P_{\text{vna}}\Bigg).\end{aligned} \tag{A2}$$

Using (A2), the impact on $\boldsymbol{\Gamma}_{\text{vna}}$ arising from variations in $\boldsymbol{\Gamma}_{\text{dut}}$ can be described by

$$\begin{aligned}\frac{\partial\Gamma_{\text{vna}}}{\partial\Gamma_{\text{dut}}} &= \frac{S_{21}^2P_{\text{vna}}^2 + 2\beta\alpha BP_{\text{vna}}^2 + \frac{a_{\text{int}}}{a_1}S_{12}\alpha P_{\text{int}}P_{\text{vna}}}{1 - S_{22}} + \cdots \\ &\quad \cdots + \frac{S_{31}^2\alpha^2B^2P_{\text{vna}}^2 + \frac{a_{\text{int}}}{a_1}S_{13}\alpha^2P_{\text{int}}P_{\text{vna}}}{1 - S_{22}} + \cdots \\ &\quad \cdots + \frac{2\Gamma_{\text{dut}}\Big(2\beta\alpha^3B^2P_{\text{vna}}^2 + S_{21}^2\alpha^2BP_{\text{vna}}^2}{1 - 2S_{22} - 2S_{22}^2\Gamma_{\text{dut}}} + \cdots \\ &\quad \cdots + \frac{\frac{a_{\text{int}}}{a_1}S_{12}\alpha^3BP_{\text{int}}P_{\text{vna}} + \frac{a_{\text{int}}}{a_1}S_{13}\alpha^4B^2P_{\text{int}}P_{\text{vna}}\Big)}{1 - 2S_{22} - 2S_{22}^2\Gamma_{\text{dut}}}.\end{aligned} \tag{A3}$$

REFERENCES

[1] J. P. Dunsmore, *Handbook of Microwave Component Measurements: With Advanced VNA Techniques*. Hoboken, NJ, USA: Wiley, 2012.

[2] M. Horibe, "Measurement uncertainty model for vector network analyzers with frequency extension modules at terahertz frequencies," *IEEE Trans. Instrum. Meas.*, vol. 66, no. 6, pp. 1605–1612, Jun. 2017.

[3] F. Mubarak, R. Romano, and M. Spirito, "Evaluation and modeling of measurement resolution of a vector network analyzer for extreme impedance measurements," in *Proc. 86th ARFTG Microw. Meas. Conf.*, Dec. 2015, pp. 1–3.

[4] M. Garelli and A. Ferrero, "A unified theory for *S*-parameter uncertainty evaluation," *IEEE Trans. Microw. Theory Techn.*, vol. 60, no. 12, pp. 3844–3855, Dec. 2012.

[5] F. A. Mubarak and G. Rietveld, "Uncertainty evaluation of calibrated vector network analyzers," *IEEE Trans. Microw. Theory Techn.*, vol. 66, no. 2, pp. 1108–1120, Feb. 2018.

[6] Z. V. Penfold-Fitch, F. Sfigakis, and M. R. Buitelaar, "Microwave spectroscopy of a carbon nanotube charge qubit," *Phys. Rev. Appl.*, vol. 7, p. 054017, May 2017.

[7] V. Ranjan *et al.*, "Clean carbon nanotubes coupled to superconducting impedance-matching circuits," *Nature Commun.*, vol. 6, p. 7165, May 2015.

[8] D. Zhang *et al.*, "Simulation and measurement of optimized microwave reflectivity for carbon nanotube absorber by controlling electromagnetic factors," *Nature Sci. Rep.*, vol. 7, pp. 1–8, Mar. 2017.

[9] C. Qiu, Z. Zhang, M. Xiao, Y. Yang, D. Zhong, and L.-M. Peng, "Scaling carbon nanotube complementary transistors to 5-nm gate lengths," *Science*, vol. 355, no. 6322, pp. 271–276, Jan. 2017.

[10] D. Wang, Z. Yu, S. McKernan, and P. J. Burke, "Ultrahigh frequency carbon nanotube transistor based on a single nanotube," *IEEE Trans. Nanotechnol.*, vol. 6, no. 4, pp. 400–403, Jul. 2007.

[11] H. Bakli, K. Haddadi, and T. Lasri, "Interferometric technique for scanning near-field microwave microscopy applications," *IEEE Trans. Instrum. Meas.*, vol. 63, no. 5, pp. 1281–1286, May 2014.

[12] S. Gu, K. Haddadi, A. E. Fellahi, and T. Lasri, "Setting parameters influence on accuracy and stability of near-field scanning microwave microscopy platform," *IEEE Trans. Instrum. Meas.*, vol. 65, no. 4, pp. 890–897, Apr. 2016.

[13] M. Randus and K. Hoffmann, "A method for direct impedance measurement in microwave and millimeter-wave bands," *IEEE Trans. Microw. Theory Techn.*, vol. 59, no. 8, pp. 2123–2130, Aug. 2011.

[14] K. Haddadi and T. Lasri, "Interferometric technique for microwave measurement of high impedances," in *IEEE MTT-S Int. Microw. Symp. Dig.*, Jun. 2012, pp. 1–3.

[15] G. Vlachogiannakis, H. T. Shivamurthy, M. A. D. Pino, and M. Spirito, "An I/Q-mixer-steering interferometric technique for high-sensitivity measurement of extreme impedances," in *IEEE MTT-S Int. Microw. Symp. Dig.*, May 2015, pp. 1–4.

[16] H. Votsi, C. Li, P. H. Aaen, and N. M. Ridler, "An active interferometric method for extreme impedance on-wafer device measurements," *IEEE Microw. Wireless Compon. Lett.*, vol. 27, no. 11, pp. 1034–1036, Nov. 2017.

[17] M. Spirito, F. A. Mubarak, R. Romano, and L. Galatro, "An interferometric iq-mixer/dac solution for active, high speed vector network analyser impedance renormalization," EU Patent PCT/NL2018/050055, Jan. 25, 2017.

[18] A. D. Sutherland and M. W. Trippe, "S-parameter equivalents of current and voltage noise sources in microwave devices," *IEEE Trans. Microw. Theory Techn.*, vol. MTT-30, no. 5, pp. 828–830, May 1982.

[19] L. Xinmeng and H. Hui, "Analyses of VNA noise floor," in *Proc. 74th ARFTG Microw. Meas. Conf.*, Nov./Dec. 2009, pp. 1–7.

[20] O. Marinov, "Noise partition in S-parameter measurement," in *Proc. 22nd Int. Conf. Noise Fluctuations (ICNF)*, Jun. 2013, pp. 1–4.

[21] J. C. Tippet and R. A. Speciale, "A rigorous technique for measuring the scattering matrix of a multiport device with a 2-port network analyzer," *IEEE Trans. Microw. Theory Techn.*, vol. MTT-30, no. 5, pp. 661–666, May 1982.

[22] M. Davidovitz, "Reconstruction of the S-matrix for a 3-port using measurements at only two ports," *IEEE Microw. Guided Wave Lett.*, vol. 5, no. 10, pp. 349–350, Oct. 1995.
[23] F. Mubarak, G. Rietveld, D. Hoogenboom, and M. Spirito, "Characterizing cable flexure effects in S-parameter measurements," in *Proc. 82nd ARFTG Microw. Meas. Conf.*, Nov. 2013, pp. 1–7.
[24] M. Spirito, L. Galatro, G. Lorito, T. Zoumpoulidis, and F. Mubarak, "Improved RSOL planar calibration via EM modelling and reduced spread resistive layers," in *Proc. 86th ARFTG Microw. Meas. Conf.*, Dec. 2015, pp. 1–5.
[25] L. Galatro, F. Mubarak, and M. Spirito, "On the definition of reference planes in probe-level calibrations," in *Proc. 87th ARFTG Microw. Meas. Conf.*, May 2016, pp. 1–4.
[26] T. J. Ypma, "Historical development of the Newton–Raphson method," *SIAM Rev.*, vol. 37, no. 4, pp. 531–551, 1995.

Faisal Ali Mubarak (M'12) was born in Lahore, Pakistan, in 1982. He received the B.Sc. degree in electrical engineering from the Rijswijk Polytechnic Institute of Technology, Rijswijk, The Netherlands, in 2006, and the M.Sc. degree in electrical engineering from the Delft University of Technology, Delft, The Netherlands, in 2009.

In 2009, he joined the VSL-Dutch Metrology Institute, Delft, where he is currently a Research Scientist with the Department of Research and Development. His current research interests include RF component measurement techniques up to millimeter-wave frequencies. In 2017, he was one of the co-founders of Vertigo Technologies, Delft, a company pioneering innovative measurement techniques and instruments.

Mr. Mubarak is a member of the International Consultative Committee for Electricity and Magnetism Working Group on Radiofrequency Quantities and the European Association of National Metrology Institutes technical sub-committee on Radiofrequencies and Microwaves (WG-RF). He was a co-recipient of the Outstanding Group Achievement Award of the Delft University of Technology and the Ritsema van Eck Prize for designing and launching the first university satellite of The Netherlands in 2007.

Rafaelle Romano was born in Salerno, Italy, in 1986. He received the M.Sc. degree in electrical engineering from the University of Naples Federico II, Naples, Italy, in 2015.

Since 2015, he has been with Delft University of Technology (TU Delft), Delft, The Netherlands, where he is currently involved in the development of the concept of the HΓ-vector network analyzer (VNA). In 2015, he joined TU Delft, as a Researcher to support the development of the first prototype of HΓ-VNA. His current research interests include the development of systems and calibration techniques for the characterization of extreme impedance devices and the characterization of devices in the millimeter-wave frequency range.

Luca Galatro (S'12) received the M.Sc. degree *(cum laude)* in electrical engineering from the University of Naples Federico II, Naples, Italy, in 2012. He is currently pursuing the Ph.D. degree at the Electronic Research Laboratory Group, Delft University of Technology, Delft, The Netherlands.

In 2017, he co-founded and was appointed as the CEO of Vertigo Technologies, Delft, a startup providing innovative test and measurement solutions for advanced, highly mismatched, and high frequency devices. His current research interests include the small and large signal characterization of electronic devices and circuits working in the millimeter-wave (mm-wave) frequency range and the development of advanced calibration and de-embedding techniques for (sub)mm-wave characterization systems.

Vincenzo Mascolo was born in Naples, Italy, in 1993. He received the B.S. and M.S. *(cum laude)* degrees in electrical engineering from the University of Naples Federico II, Naples, in 2015 and 2017, respectively. In 2017, he completed his thesis project at the Delft University of Technology, Delft, The Netherlands, and the VSL-Dutch Metrology Institute, Delft.

His current research interests include mm-wave extreme impedance measurements, electromagnetic imaging, and dielectric spectroscopy techniques.

Gert Rietveld (M'10–SM'12) was born in Hardinxveld-Giessendam, The Netherlands, in 1965. He received the M.Sc. *(cum laude)* and Ph.D. degrees in low temperature and solid-state physics from the Delft University of Technology, Delft, The Netherlands, in 1988 and 1993, respectively.

In 1993, he joined the VSL-Dutch Metrology Institute, Delft, The Netherlands, where he is currently a Chief Metrologist with the Research and Development Department. His current research interests include the breadth of electromagnetic precision measurements, including the development of power measurement systems and electrical quantum standards, in particular, the quantum Hall resistance standard.

Dr. Rietveld is a member of the International Committee for Weights and Measures (CIPM) and the President of its Consultative Committee for Electricity and Magnetism (CCEM). He is also the Chair of the Energy Task Group of the European Association of National Metrology Institutes (EURAMET), the Founding Chair of the EURAMET Subcommittee on Power and Energy, and a member of several CCEM, EURAMET, International Council on Large Electric Systems, and IEEE Working Groups.

Marco Spirito (S'01–M'08) received the M.Sc. degree *(cum laude)* in electrical engineering from the University of Naples Federico II, Naples, Italy, in 2000, and the Ph.D. degree from the Delft University of Technology, Delft, The Netherlands, in 2006.

From 2000 to 2001, he was a Guest Researcher with Infineon Technologies, Munich, Germany. In 2006, he joined the Department of Electronics and Telecommunications Engineering, University of Naples Federico II. In 2008, he became an Assistant Professor with the Electronics Research Laboratory, Delft University of Technology, where he has been an Associate Professor since 2013. In 2010 and 2017, he was one of the co-founders of Anteverta-MW, Eindhoven, The Netherlands, and Vertigo Technologies, Delft, respectively, two companies pioneering innovative measurement techniques and instruments. His current research interests include the development of advanced passive components and building blocks operating in the millimeter and submillimeter frequency ranges, the development of characterization setups and calibration techniques for millimeter-waves (mm-wave) and submillimeter waves, and the design and integration of mm-wave sensing systems.

Dr. Spirito was a recipient of the Best Student Paper Award for his contribution to the 2002 IEEE Bipolar/BiCMOS Circuits and Technology Meeting. He was the recipient of the IEEE Microwave Theory and Techniques Society Microwave Prize in 2008, was a co-recipient of the Best Student Paper Award of the IEEE Radio Frequency Integrated Circuits 2011, the GAAS Association Student Fellowship in 2012, and the Best Student Paper Award in Second Place at the International Microwave Bio-Conference 2018.